Threshold effects in the development of highly ionized plasma channels in a pulsed nanosecond discharge in air at pressures of 100–760 Torr

E. V. Parkevich,[1,*] A. I. Khirianova,[1] K. V. Shpakov,[1] T. F. Khirianov,[1,2] and N. A. Popov[3]

[1]*P. N. Lebedev Physical Institute of the Russian Academy of Sciences, 53 Leninskiy Prospekt, 119991 Moscow, Russia*

[2]*Moscow Institute of Physics and Technology, Institutskiy Pereulok 9, Dolgoprudny, 141700 Moscow Region, Russia*

[3]*Skobeltsyn Institute of Nuclear Physics, Moscow State University, 119991 Moscow, Russia*

(Received 22 June 2025; accepted 3 December 2025; published 30 December 2025)

The formation processes of highly ionized plasma channels (filaments), with an electron concentration of $N_e \sim 10^{18}$–10^{19}cm^{-3}, in a pulsed nanosecond discharge in air at a pressure of 100–760 Torr are investigated. The studies are carried out for millimeter-sized gaps with a point cathode and flat anode. It is established that explosive processes at the cathode give rise to the emergence of an ionization wave propagating toward the anode with a velocity of $\sim 10^6$–10^7 cm/s and initiating the development of highly ionized filaments. The wave's propagation velocity is practically independent of the air pressure. At pressures 400–760 Torr, the ionization wave front is unstable and splits into numerous microchannels with typical diameters of $\sim$20 μm and electron concentrations $N_e = (1\text{–}5) \times 10^{19}\text{cm}^{-3}$. The microchannel formation ceases to be observed when the air pressure decreases from 400 to 300 Torr, whereas the discharge development occurs mainly through the development of a uniform highly ionized plasma filament. A decrease in pressure entails the drop in the maximum values of electron concentrations, which, however, are close to the values corresponding to complete ionization. Theoretical estimates of characteristic filamentation times are presented together with the analysis of the possible mechanism responsible for generating plasma with a high degree of ionization. The findings can be helpful in refining the models of plasma-chemical kinetics and the formation mechanisms of a system of highly ionized microchannels in high-pressure discharges at nanosecond times.

DOI: 10.1103/bq1x-2p4t

I. INTRODUCTION

The study of the filamentation processes of a pulsed nanosecond discharge in an air environment is relevant for many applications of the gas discharge physics [1]. These processes are capable of radically changing both the spatial structure of the discharge and the plasma-chemical kinetics in single channels [2–4]. The filamentation processes are also assumed to be scaled when increasing the discharge gap length [5] and influence the formation of long spark discharges [6–9]. As part of the filamentation process, the appearance of thin plasma filaments (tens to hundreds of micrometers in diameter) with a high degree of ionization (units to tens of percent) is possible. It was shown that certain filaments can represent almost fully ionized air plasma (with an electron concentration of $N_e > 10^{19}\text{cm}^{-3}$) close to the state of local thermodynamic equilibrium [10]. As the transition of the discharge to the filamentary regime occurs, the gas temperature in the discharge channel can increase to tens of thousands of degrees in a matter of nanoseconds [2]. During the transition, the emission spectrum of the discharge channel, which at the initial stage is characterized by molecular bands of N_2, is then followed by continuous emission with the appearance of broadened lines of atoms (N, O) and atomic ions (N^+) [11–13]. However, in spite of various investigations in this research field, a number of aspects related to the filamentation mechanism still represent an open problem requiring careful analysis. In particular, this concerns the formation of a complex filamentary microstructure in the discharge channel–plasma channels with a diameter of $\sim$10–20 μm and a length of several millimeters [14–16]. It is assumed that the appearance of microchannels of highly ionized plasma is driven by the development of ionization instabilities [17–19], which significantly depend on the key conditions of the discharge formation. It was shown that, when varying the energy input into the discharge medium (current through the discharge gap) [20] or creating preionization [21], the dynamics of the microstructure development in an electric spark changes. In particular, at currents less than 100 A, the formation of microchannels from the cathode is not observed [20], as in the case when seed preionization is initially created in the zone of the microchannel formation [21]. Remarkably, in the recent study [22] it was reported that in a gas discharge medium consisting of pure nitrogen at pressures below $\sim$200 Torr, the microstructure formation is not registered, as in air at pressures less than $\sim$300 Torr. It should be noted that in modern literature there is a lack of quantitative data on the dynamics of the parameters of highly ionized filaments obtained with a high temporal (better than 1 ns) and spatial (several micrometers) resolution when varying the key conditions of the discharge formation. This fact challenges the development of models of fast plasma formation processes that would be able to comprehensively explain the fast fine-scale spark filamentation mechanism–microstructure formation.

*Contact author: parkevich@phystech.edu

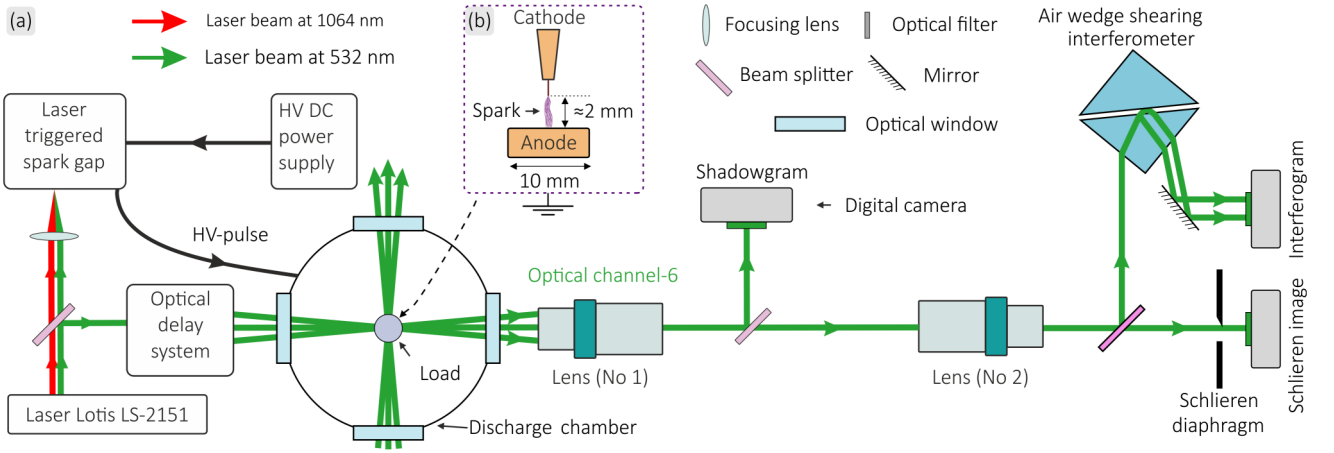

FIG. 1. (a) Schematic illustration of the experimental setup and diagnostics used. (b) Air discharge gap with a point cathode probed by a laser pulse.

In this study, we investigated in detail the development features of highly ionized plasma channels formed in a pulsed nanosecond discharge in air at pressures from units of Torr to 760 Torr. The measurements were carried out using the methods of picosecond laser probing of plasma. Based on the mathematical processing of interferograms, supplemented with the results of the analysis of laser shadowgrams and schlieren images registered simultaneously in each discharge event, we discovered qualitatively new structural transitions between the regimes of the development of filaments at low air pressures. In particular, we revealed the important role of the generation of highly ionized near-cathode plasma and the threshold (by pressure) nature of the formation of microchannels in the discharge gap (far from the cathode). The results of the study can be useful in constructing consistent models of the observed plasma formation phenomena depending on a wide range of experimental conditions.

II. EXPERIMENTAL SETUP AND DIAGNOSTICS

In experiments, we used a previously developed setup, see Fig. 1(a), based on a high-voltage cable generator of voltage pulses with an amplitude of up to 25 kV, a rise time ≈4 ns and duration of ≈ 40 ns at a maximum generator current of about 300 A [23]. The generator was synchronized with a picosecond Nd: YAG laser LS-2151 with an accuracy better than 1 ns by switching a laser-triggered spark gap [24]. The laser produced radiation pulses with an energy of up to 80 mJ at wavelengths of 1064 and 532 nm, with a pulse duration being 70 ps at 532 nm. The high-voltage pulse of the generator was supplied into the discharge chamber to a discharge gap with the electrode geometry "point cathode–flat anode"; see Fig. 1(b). As a point cathode, we used a copper wire with a diameter of 100 μm and a length of several millimeters. The gap between the cathode tip and flat anode (copper cylinder with a base diameter of 10 mm) was ≈2 mm. The employment of a point cathode made it possible to reduce the sporadic nature of the discharge development in space, since the formation of highly ionized filaments always started from the cathode tip. In addition, owing to the precise focusing of the optical lens system on the region with the thin cathode, an optimal regime of laser photography of plasma structures was achieved from the point of view of the subsequent employment of the geometrical optics approximation in the image processing procedure [25].

The discharge development was investigated in the range of dry air pressures from units of Torr to 760 Torr. The air pressure was controlled by a Televac CC-10 digital vacuum gauge with an accuracy of ± 5% (over the entire pressure range). To image the highly ionized plasma formation, we used a laser diagnostic system developed earlier in Ref. [23]. The system provides multi-imaging based on six laser beams at 532 nm that probe the discharge gap with a relative delay of several nanoseconds in a single shot produced by the high-voltage generator. In the current research, we mainly present the images registered by using the sixth beam. However, the data obtained using the other beams were also used to determine certain characteristics of the observed plasma and its dynamics. The designs of optical channels for each of the beams were identical to that shown in Fig. 1(a). The energy of each beam did not exceed several mJ, and the beam's diameters were ∼1 cm. In the optical channel in Fig. 1(a) the laser beam was recorded by high-quality "Era-14" lenses having a spatial resolution better than 2–3 μm. Simultaneous registration of interferograms, shadowgrams and schlieren images with an approximately ten-fold magnification was implemented in the optical channel. All the images were recorded using Canon1200 digital cameras (CMOS sensor 22.2 × 14.7 mm, 12.2 effective megapixels) combined with glass-optical filters to attenuate the discharge glow. The image exposure time was 70 ps. The discharge current and voltage were detected by a coaxial shunt and resistive voltage divider both having a subnanosecond temporal resolution [16]. The moments of laser probing of the discharge were controlled by a Thorlabs DETO25A photo-detector (with a rise time of 150 ps). The signals of all detectors were registered by using a LeCroy Wave Master 8620A oscilloscope (6 GHz, 20 GSa/s).

III. IMAGE PROCESSING PROCEDURE

The quantitative information about the geometric dimensions of plasma structures and electron density distributions

was obtained through mathematical processing of interferograms. The processing results were further refined by analyzing schlieren images and shadowgrams. Interferograms were recorded using a shearing interferometer based on an air microwedge between two faces of rectangular prisms [23,26,27]. In each shot, two interferograms were recorded: with and without (reference) an object. When processing both interferograms by using the dedicated procedures [28,29], a two-dimensional map of the phase shift introduced by the plasma into the passing laser radiation was constructed. The relationship between the radiation phase shift and dispersion part of the plasma dielectric permittivity was considered in the geometrical optics approximation [25]

$$\delta\phi(x,\rho) = \frac{k}{2}\int_0^x \tilde{\varepsilon}(\eta,\rho)d\eta, \tag{1}$$

$$\tilde{\varepsilon} = -\frac{\omega_{pe}^2}{\omega^2+\nu_{\text{eff}}^2}(1+i\nu_{\text{eff}}/\omega), \tag{2}$$

$$\omega_{pe} = \sqrt{4\pi e^2 N_e/m_e}, \tag{3}$$

where ρ is the two-dimensional variable introduced for the transverse y and z variables; ω_{pe} and $\omega = 3.5\times10^{15}\text{s}^{-1}$ are the plasma frequency and the frequency of the probing laser radiation; e and m_e are the electron charge and mass. The parameter ν_{eff} describes the effective frequency of elastic collisions of electrons in a gas-discharge medium defined as the sum of the frequencies of electron collisions with neutral particles ν_{em}, ions ν_{ei}, and electrons ν_{ee}. The parameter x is the distance at which the field of the transmitted radiation behind the object is detected. The plane with the coordinate $x = 0$ corresponds to the object's input plane. Based on the estimates presented below in this research (see also in Ref. [30]), one can show that for the spark plasma with electron concentrations as high as $N_e \approx 5\times10^{19}\text{cm}^{-3}$ and electron temperatures $T_e = 1-5$, the high-frequency approximation $(\nu_{\text{eff}}/\omega)^2 \ll 1$ is well satisfied, owing to which expression (2) takes the form $\tilde{\varepsilon} = -\omega_{pe}^2/\omega^2$.

Let us clarify that in the presence of a purely plasma medium we have $\tilde{\varepsilon} < 0$ and $\delta\phi < 0$. When solving the inverse diffraction problem, the experimental distribution of the phase shift $\delta\phi^{\text{exp}}$ (extracted from the phase shift map for a certain slice) is smoothed and symmetrized. Next, the smooth symmetrized distribution $\delta\phi^*$ is used in the numerical solution of the equation system obtained within the framework of the Abel-Fourier-Hankel transform cycle [31] successively applied to Eq. (1):

$$\mathcal{F}[\delta\phi^*(y)](f_y) = 2\int_0^{+\infty}\delta\phi^*(y)\cos(2\pi y f_y)dy, \tag{4}$$

$$\tilde{\varepsilon}(r) = \frac{4\pi}{k}\int_0^{+\infty}\mathcal{F}[\delta\phi^*(y)](f_y)J_0(2\pi r f_y)df_y. \tag{5}$$

Herein, we have the two-dimensional variable $r-$ the modulus of the radius-vector drawn from the symmetry center of the phase shift profile $\delta\phi^*(y)$, the zero-order Bessel function $J_0(2\pi r f_y)$, the Fourier spectrum $\mathcal{F}[\delta\phi^*(y)](f_y)$ of the phase shift function $\delta\phi^*(y)$, the spatial frequency f_y introduced for the transverse variable y. Numerical simulations of Eqs. (4) and (5) showed that the reconstruction error of function $\tilde{\varepsilon}$ can be estimated from above as $\text{NRMSD}[\delta\phi^{\text{exp}};\delta\phi^*]+2\%$, where the normalized root-mean-square deviation,

$$\text{NRMSD}[\delta\phi^{\text{exp}};\delta\phi^*] = \frac{\left(\sum_i^{N_y}[\delta\phi^{\text{exp}}(y_i)-\delta\phi^*(y_i)]^2\right)^{1/2}}{\max\{\delta\phi^{\text{exp}}\}-\min\{\delta\phi^{\text{exp}}\}}, \tag{6}$$

is introduced and appears as an approximation error of functions $\delta\phi^{\text{exp}}$ and $\delta\phi^*$. Parameter N_y equals the efficient number of pixels of the CMOS matrix along the drawn slice.

Thus, in this research, we present the electron concentration profiles reconstructed with an error of $\text{NRMSD}[\delta\phi^{\text{exp}};\delta\phi^*]+2\%$ and with a sampling step of $\approx$2.3 μm, which characterizes the spatial resolution of the optical system.

IV. RESULTS OF EXPERIMENTAL MEASUREMENTS

Let us turn to the results of laser photography in Figs. 2–4. Herein there are interferograms, schlieren images, and shadowgrams registered at 532 nm in shots 1–7 at different air pressures (100–760 Torr) after Δt (ns) the onset of the electrical breakdown–the beginning of a sharp increase in the discharge current (∼200 A/ns) and a drop in the discharge voltage. The current and voltage waveforms for shots 1–7 are shown in Fig. 5. All types of the images in Figs. 2–4 were obtained simultaneously in each shot at the moment of the gap probing, which, as a rule, coincided with the developed stage of the filament between both electrodes (on average, at $\Delta t \sim 10$ ns). The comparison in this case is made with a typical filament pattern obtained in atmospheric air, when a resultant filament has time to form between the electrodes and has a clearly resolvable microstructure. Thus, without changing the basic conditions of laser measurements (in particular, the time stage of observations), we traced the key changes in the dynamics of highly ionized plasma in the discharge gap with varying the air pressure. The data on the registered electron concentrations depending on the air pressure are presented in Figs. 6(a) (range 100–400 Torr), 6(b) (range 500–760 Torr), and 6(c) (dependence of the detected maximum electron concentration on the air pressure). Additional images of the studied discharge at air pressures of 500–760 Torr, which were taken for processing, are given in Fig. 7.

A. Plasma formation in air at $P = 760$ Torr

The development of a spark channel from a point cathode in atmospheric air was described in detail earlier in Refs. [16,30,32]. In Ref. [30] it was shown that the initiation of a highly ionized channel (channels) starts from the appearance of a cathode spot with an electron density of at least 10^{19}cm^{-3} and a size of about 10–20 μm. Notably, these representations were obtained on a timescale of approximately 0.5–1 ns relative to the instant of the discharge gap breakdown with a spatial resolution of the diagnostic system of 2–3 μm. Today, it is not yet completely clear what kind of structure is contained in the cathode spot, what the true electron density distributions of the cathode spot plasma are, and from what minimum size the process of its generation begins. We refer these questions to future studies.

As a rule, after several nanoseconds, due to the explosive expansion of the near-cathode plasma, the cathode spot is

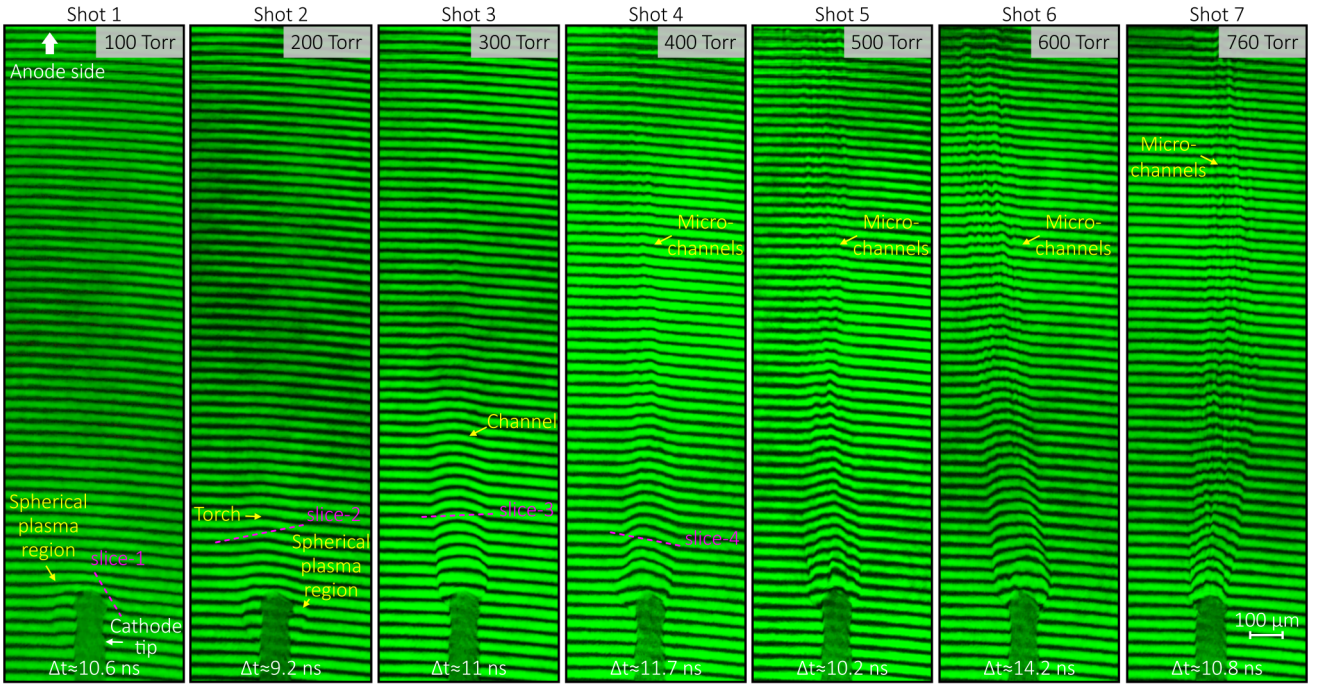

FIG. 2. Laser interferograms of the discharge gap registered at 532 nm in shots 1–7 at different air pressures (100–760 Torr) after the onset of the electrical breakdown. The parameter Δt (ns) denotes the time passed from the breakdown moment to the instant of laser probing the discharge gap. The processing results obtained for the slices 1–4 drawn in the interferograms are presented in Fig. 6(a).

transformed into a spherical plasma zone with a diameter of about 100 μm possessing very high electron density gradients [33]. In the shell (≈20 μm in width) of such a zone, electron densities of up to (5–6) $\times$ 10^{19}cm^{-3} can be reached. From the boundaries of the spherical plasma zone an ionization wave starts to propagate toward the anode, which travels with a characteristic velocity close to 10^7 cm/s and paves the way for the development of a subsequent highly ionized channel (filament) in the direction of the anode. Here, we associate the ionization wave front with the head of the growing spark channel (filament), wherein ionization and dissociation reactions occur intensively. The boundary of the channel's head is

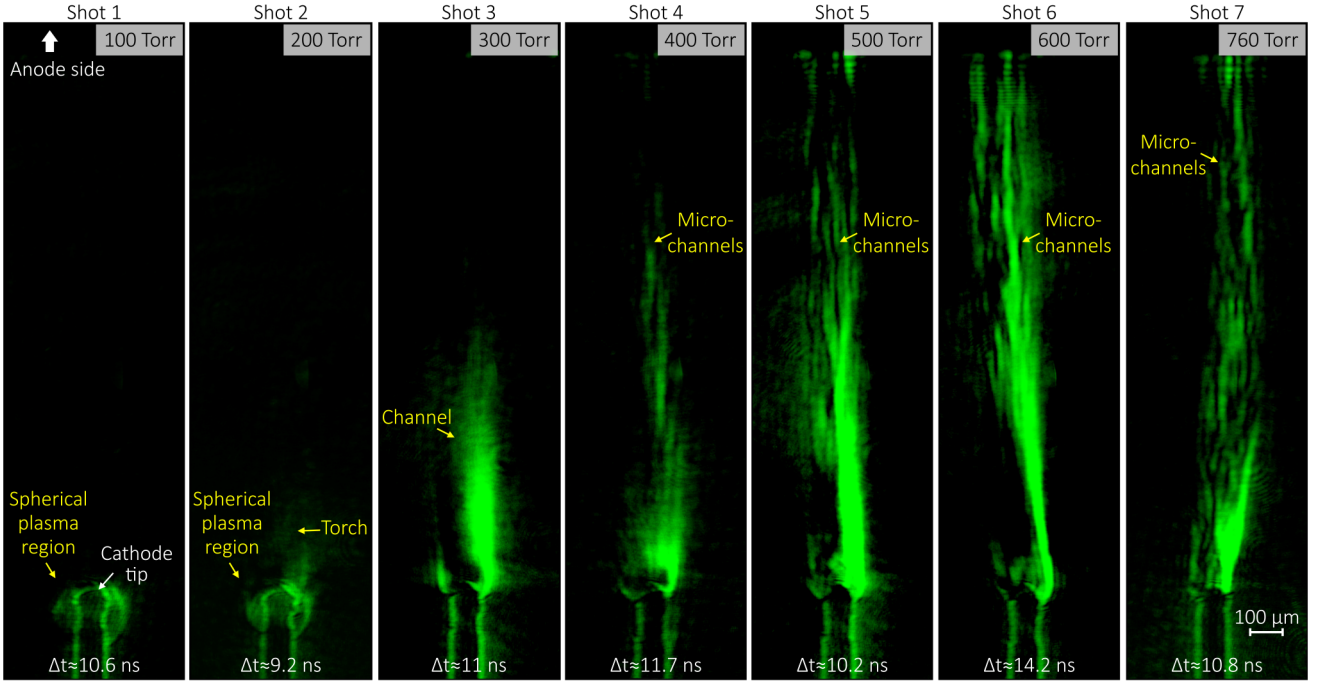

FIG. 3. Laser schlieren images of the discharge gap registered at 532 nm in shots 1–7 at different air pressures (100–760 Torr) after the onset of the electrical breakdown.

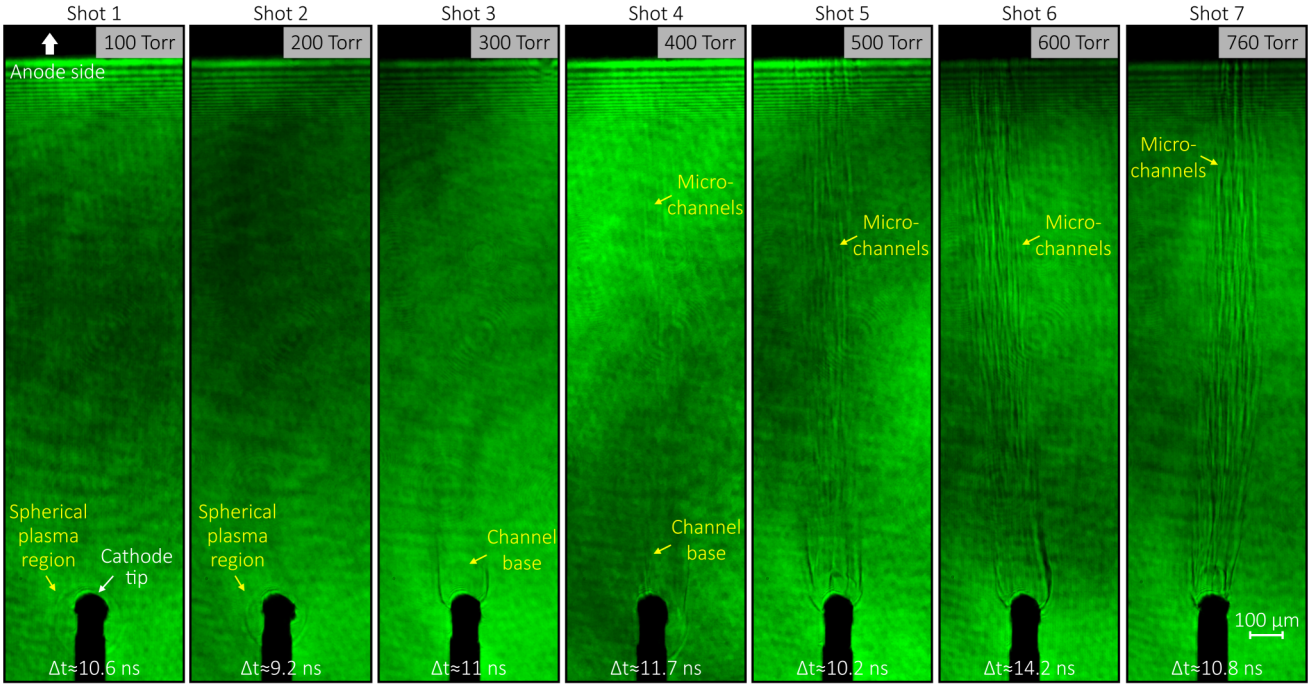

FIG. 4. Laser shadowgrams of the discharge gap registered at 532 nm in shots 1–7 at different air pressures (100–760 Torr) after the onset of the electrical breakdown.

defined based on the processed laser interferogram data further refined by the analysis of schlieren images. This boundary is interpreted as the zone where a highly ionized plasma is generated via the stepwise dissociation and ionization mechanisms (will be described below) at an electron concentration that exceeds the sensitivity threshold ($N_e^{\min}$) of the employed laser diagnostic methods–the minimum resolvable electron density. For example, for plasma on a spatial scale of $D = 200\,\mu$m the threshold can be estimated as $N_e^{\min} = k/(A \times D \times \lambda) \approx 10^{18}\text{cm}^{-3}$. Here we have $A = 4.49 \times 10^{-14}$ cm, $\lambda = 0.532 \times 10^{-4}$ cm, and $k \approx 0.05$ is the minimum registered phase shift in the interferogram, which takes into account the influence of the spatial resolution of the optical system, the interferogram pixelation, and the noise on the extracted phase shift map.

A feature of the propagated ionization wave is the fact that it is unstable and begins to break up into separate microchannels at a distance of several hundred micrometers relative to the cathode tip. Microchannels have typical diameters of about 20 μm, and the microchannels' plasma with electron concentrations $N_e = (1-5) \times 10^{19}\text{cm}^{-3}$ can be close to the state of complete ionization [16], see also the results obtained for microchannels growing from a point anode [34]. Note that high values of the electron density, up to $(5 \pm 0.3) \times 10^{19}\text{cm}^{-3}$, are also observed in the relatively homogeneous part of the developing filament; see Fig. 6(b). Quantitative data on the electron density in the filament were obtained from the images shown in Fig. 7. Further formation of the resultant filament between the electrodes typically occurs through the development of a system of multiple microchannels. Microchannels branch, the degree of ionization increases in them, the microchannel number rises over time–all this together determines the fine-scale spark filamentation process [16]. As a result, the resultant filament, while being several hundred micrometers in diameter, turns out to consist of dozens of microchannels of highly ionized plasma. This is clearly demonstrated by the images in Figs. 2–4 obtained under atmospheric air conditions. The microstructure has a high contrast in the laser shadowgram and is clearly visible in the interferogram and schlieren image. In the case of schlieren imaging, the pattern of the plasma object is obtained due to refraction of a laser beam on high electron density gradients [35,36]. On average, the values of the growth rate of microchannels were registered in the range from $\sim 10^7$ to $\sim 10^8$ cm/s. In a number of shots, it was possible to register the growth of single microchannels with a rate as high as $\sim 10^9$ cm/s. Note that the growth rate of microchannels can vary from shot to shot.

B. Plasma formation in air at $P = 500$–600 Torr

When the air pressure was reduced to 500 Torr, no fundamental changes in the development of the microstructure inside the resultant filament were detected, with one exception: the contrast of the shadow image of the microstructure in the laser shadowgram drops down. This is probably due to the fact that, when proceeding to 500 Torr, the maximum value of the plasma electron density that can be reached in the medium decreases slightly, since the concentration of the original air molecules decreases. For example, in atmospheric air we have $N = 2.7 \times 10^{19}\text{cm}^{-3}$ molecules. With complete dissociation and single ionization one can reach an electron density of up to $N_e^{\text{thr}} = 5.4 \times 10^{19}\text{cm}^{-3}$ ('threshold'). Similar values of electron density were observed earlier in Refs. [37,38]. At $P = 500$ Torr we have $N = 1.78 \times 10^{19}\text{cm}^{-3}$ and $N_e^{\text{thr}} = 3.55 \times 10^{19}\text{cm}^{-3}$, whereas the registered maximum electron

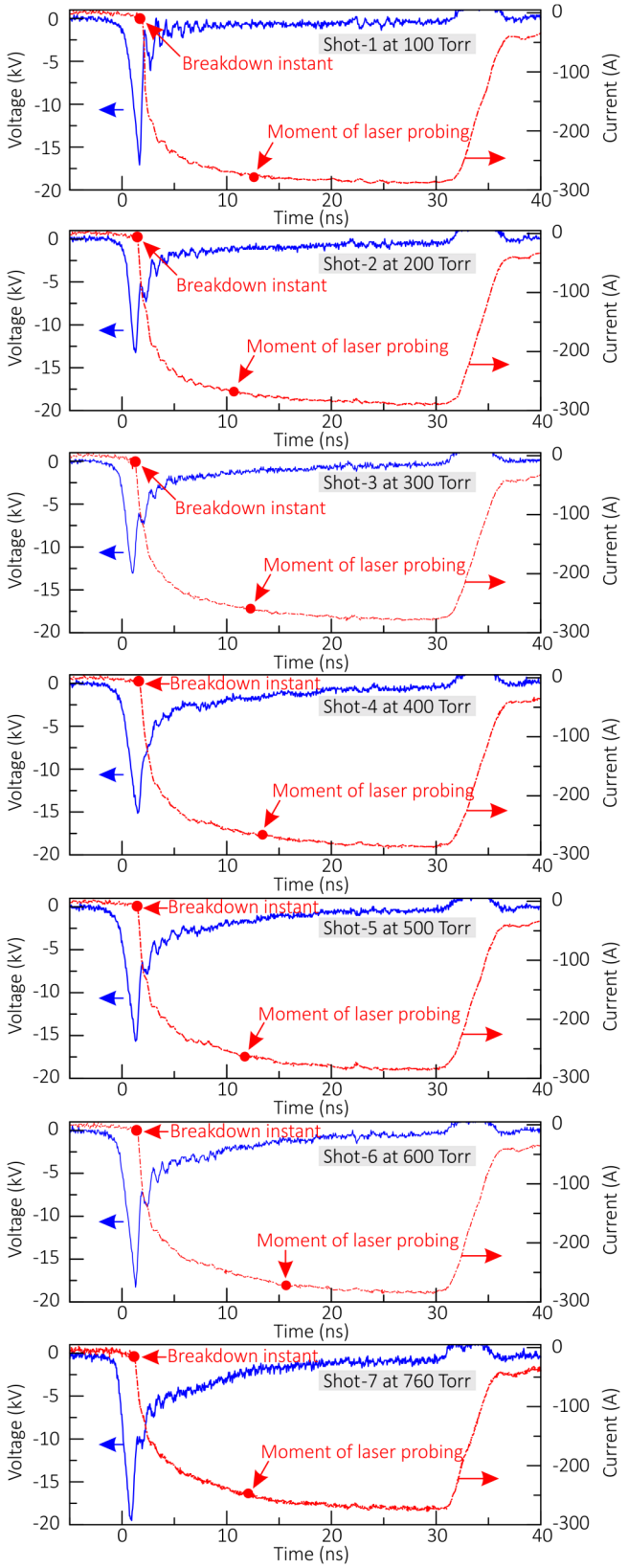

FIG. 5. Discharge voltage and current waveforms in shots 1–7. In each shot the gap breakdown instant and moment of laser probing are marked.

concentrations are close to N_e^{thr}, see Fig. 6(b). Note that slightly higher electron densities, $N_e^{\max} = (4.75 \pm 0.25) \times 10^{19}\text{cm}^{-3}$, relative to N_e^{thr} are observed at $P = 600$ Torr, although the tendency to decrease in $N_e^{\max}$ with decreasing air pressure remains.

C. Plasma formation in air at $P = 400$ Torr

When proceeding to the air pressure of 400 Torr, the growth rate of microchannels decreases (the process of the microstructure formation in the discharge channel slows down), on average to $\approx(1.8\text{–}4.4) \times 10^7$ cm/s, which, however, is higher than the typical propagation velocity of the ionization wave from the cathode, on average $\approx(5\text{–}7.8) \times 10^6$ cm/s. At a pressure of about 400 Torr, the microstructure continues to be resolved in the laser interferogram and schlieren image, but in the shadowgram the microstructure contrast drops sharply. As a result, it is practically invisible. In this case, the high contrast in the shadowgram is at the base of the growing filament, wherein sufficiently high electron density gradients are reached, and accumulation of diffraction effects occurs when coherent laser radiation passes through an inhomogeneous plasma medium [39]. The typical electron density of the observed plasma decreases. For example, the mathematical processing of the interferogram in Fig. 6(a) for the drawn slice 4 showed that the value of the maximum electron density is $N_e^{\max} = (1.93 \pm 0.16) \times 10^{19}\text{cm}^{-3}$, which is ≈68% of $N_e^{\text{thr}} \approx 2.84 \times 10^{19}\text{cm}^{-3}$ (at $P = 600$ Torr). Let us clarify that for the analysis of the plasma electron density we intentionally selected a relatively homogeneous and developed section of the growing filament, wherein the electron density had already reached its maximum value and significant structural changes are not observed. In this case, the processing of the phase shift profiles was as correct as possible.

D. Structural changes in filaments upon transition to $P = 300$ Torr

A distinctive feature of the transition to 300 Torr is the fact that the formation of highly ionized microchannels ceases to be traced along the filament with the achieved sensitivity of laser probing methods at 532 nm. Weak inhomogeneities in the plasma (low gradients of the electron density) indicated by the schlieren image turn out to be unresolvable in the interferogram and even more so in the shadowgram. Typically, at $P = 300$ Torr we observe the development of a relatively homogeneous filament with a smooth electron density profile at the periphery, see the data obtained for slice 3 in Fig. 6(a). Note that, when decreasing the air pressure from 760 to 300 Torr, the filament diameter increases on average from about 100 to 200 μm. The maximum electron density is detected at the level of $N_e^{\max} = (1.76 \pm 0.06) \times 10^{19}\text{cm}^{-3}$; this is ≈83% of $N_e^{\text{thr}} \approx 2.13 \times 10^{19}\text{cm}^{-3}$ (at $P = 300$ Torr). At a pressure of 300 Torr high gradients of an electron density are often observed in the cathode region and visualized as complex inhomogeneities with sharp changes in the intensity of the shadow pattern. In addition, a synchronous formation of a number of highly ionized plasma channels originating from the cathode can be observed, see Fig. 8. The analysis of the parameters of such channels (their diameters and development patterns were examined) showed that they cannot pretend to be microchannels, which are observed at higher

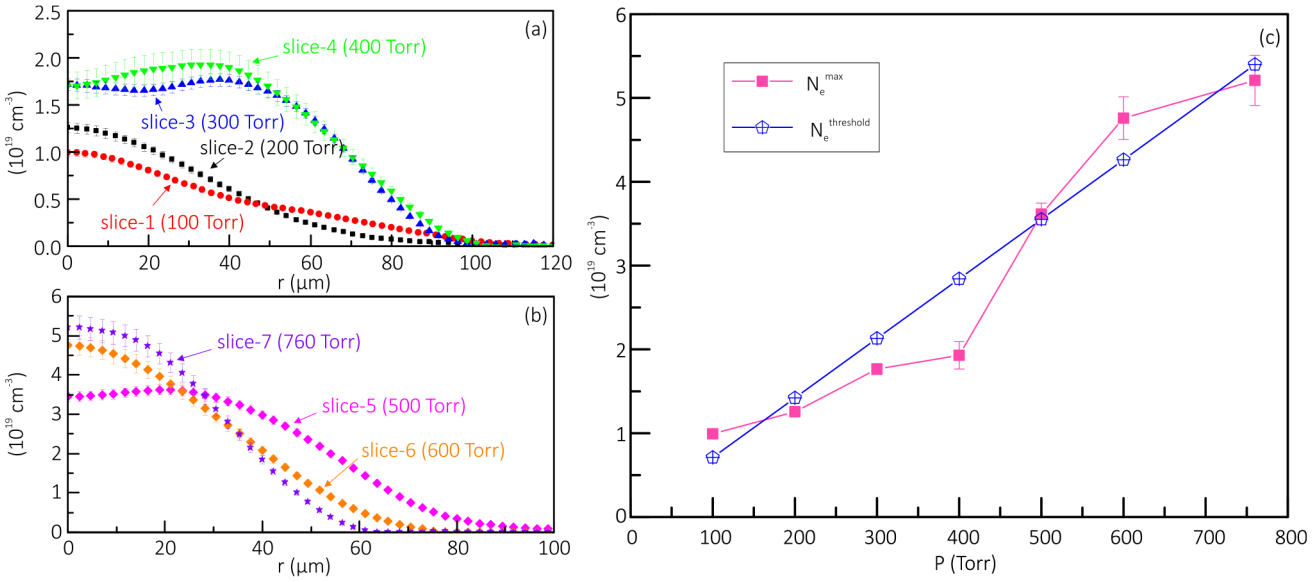

FIG. 6. (a) Distributions of the plasma electron density N_e reconstructed for the slices 1–4 drawn in the interferograms in Fig. 2 for the case of pressures of 100–400 Torr. (b) Distributions of the plasma electron density N_e reconstructed for the slices 5–7 drawn in the interferograms in Fig. 8 for the case of pressures of 500–760 Torr. The parameter r is the distance measured from the found characteristic center of symmetry in the distribution of the phase shift profile $\delta\phi^*$. (c) Dependence of the maximum electron density $N_e^{\max}$ registered in a certain cross-section of a filament on the air pressure P (Torr). The curve N_e^{thr} is the electron concentration obtained at a given pressure in the case of complete dissociation and single ionization of the air medium.

pressures. The fundamental difference between them is that the microchannels at high pressures are narrower, their number at the base of the resultant channel is greater, and they are located close to each other (microstructure is channeled). In the images in Fig. 8 the diameters of the secondary channels from the cathode are ≈107, ≈81, ≈56, ≈100, and ≈105 μm. On average, the growth rate of the filament from the cathode at $P = 300$ Torr is from $\approx 6.5 \times 10^6$ to $\approx 1.4 \times 10^7$ cm/s, which is similar to the propagation velocity of the ionization wave at higher pressures.

E. Plasma generation in air at $P = 100$–200 Torr

At air pressures below 300 Torr any development of highly ionized plasma in the form of an extended microstructure (from the cathode to the anode) is not observed in principle. Moreover, the picture of the development of the entire discharge changes radically: At $P = 100$–200 Torr we often observe explosive initiation of highly ionized plasma on the lateral surface of the point cathode, below its tip at a distance of about 300 μm. Note that at high pressures highly ionized plasma emerges in the form of a micron-sized cathode spot, which subsequently gives rise to the development of an ionization wave. The spot, however, appears exclusively at the top of the cathode tip, where the highest value of the electric field strength is expected to be reached, not below it. One can assume that at pressures of no more than 200 Torr the regime of the electron emission from a point cathode is close to that inherent in a vacuum diode with a point cathode. Due to the influence of a strong radial component of an electric field together with the spatial charge of the emitted electron flow, for the thin point cathode the electron emission from an extended part of the lateral surface of the cathode prevails, wherein an intensive production of plasma of the cathode substance is expected partially to screen the energy input directly into the cathode tip [40,41]. The near-cathode plasma within a few nanoseconds after its origination, while possessing high electron density gradients, expands spherically around the cathode tip with a characteristic velocity close to 10^6 cm/s [42]. One of the distinct differences in the formation dynamics of highly ionized plasma for the cases of $P = 100$ and 200 Torr is that at 200 Torr the development of a kind of an embryo of a homogeneous filament in the anode direction is observed (in Figs. 2–4 it is marked as a "torch"). Its growth rate within the considered timescales is $\approx (5$–$7.8) \times 10^6$ cm/s.

Thus, one can conclude that the propagation velocity of the ionization wave from the generation region of the primary highly ionized near-cathode plasma changes slightly with decreasing the air pressure. The fundamental differences in the dynamics of the propagating ionization wave with decreasing the air pressure consist only in the fact that the maximum values of the plasma electron density registered in local areas of the filament far from the cathode tip decrease. For example, the time stage shown in Figs. 2–4 characterizes the plasma of the growing torch (far from the cathode and spherical plasma region around the cathode tip) with electron density values at the maximum of up to $N_e^{\max} = (1.25 \pm 0.05) \times 10^{19}\text{cm}^{-3}$; this is ≈88% of $N_e^{\text{thr}} \approx 1.42 \times 10^{19}\text{cm}^{-3}$ (at $P = 200$ Torr), see the data in Fig. 6(a) obtained for the slice 2.

F. Features of the near-cathode plasma generation at $P \leqslant 100$ Torr

As shown in Ref. [34] aimed at investigating in detail the characteristics of the cathode plasma during the first

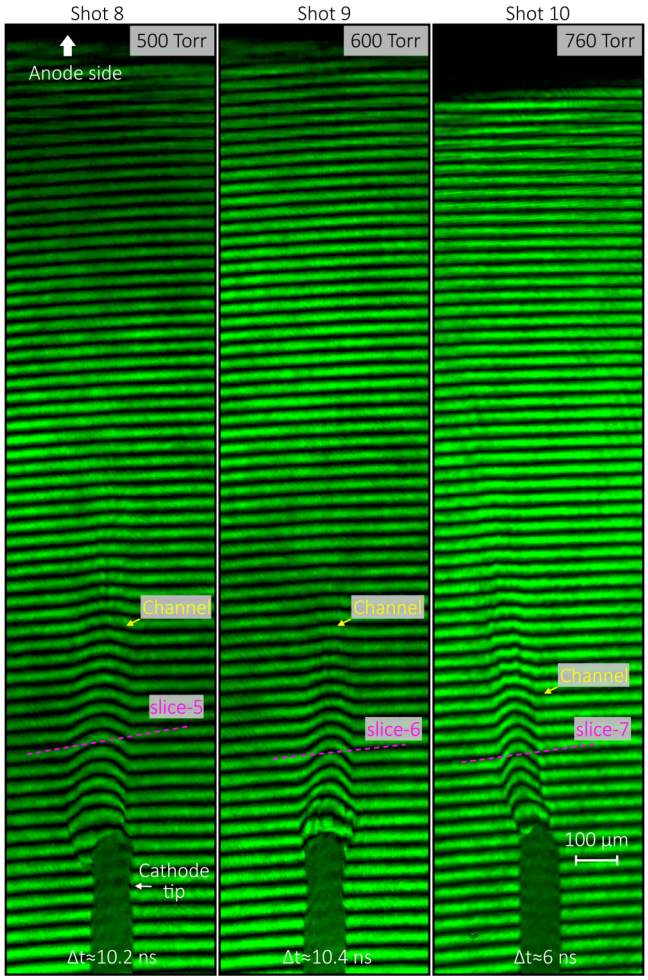

FIG. 7. Interferograms (obtained in shots 8–10) of a highly ionized filament observed at pressures of 500–760 Torr at different times after the gap breakdown. The processing results obtained for the slices 5–7 drawn in the interferograms are presented in Fig. 6(b).

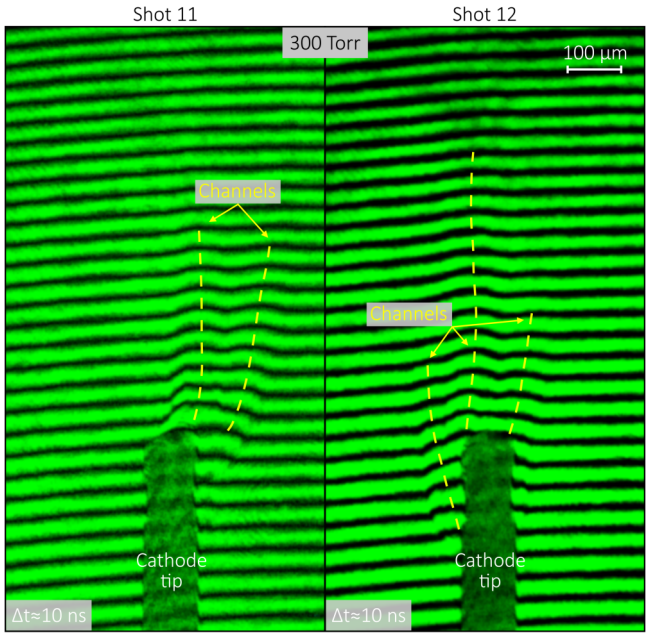

FIG. 8. Several highly ionized plasma channels originating from the point cathode in air at $P = 300$ Torr.

nanoseconds of its evolution at $P = 100$ Torr, the maximum values of the electron density can be quite high near the cathode surface, up to $N_e \approx 6 \times 10^{19}\text{cm}^{-3}$. These values are almost ten times higher than the characteristic threshold for the electron concentration in plasma obtained exclusively from air particles. Let us clarify that in air at $P = 100$ Torr we have $N = 3.55 \times 10^{18}\text{cm}^{-3}$ molecules, and the expected maximum electron density values obtained with complete dissociation and single ionization of air particles are limited from above by $N_e^{\text{thr}} = 7.1 \times 10^{18}\text{cm}^{-3}$. Even at a later stage of the near-cathode plasma evolution, when the plasma is represented in the form of a spherical formation Figs. 2–4 enveloping the top of the point cathode, electron densities at maximum up to $N_e^{\max} = (0.99 \pm 0.04) \times 10^{19}\text{cm}^{-3}$ are observed, see the data in Fig. 6(a) obtained for the slice 1. The described facts indicate that the observed cathode plasma near the cathode tip is mostly represented by ionized vapors of sublimated cathode material, which is generated in microscales of the cathode surface because of the transition to the explosive electron emission [43] at sufficiently high energy input powers (greater than $10^8\text{W} \times \text{cm}^{-2}$ [44]). By the way, the estimates in Ref. [34] showed that the near-cathode plasma, when excluding the maximum contribution to the electron density provided by the air environment, corresponds to the sublimation of the order of several cubic micrometers of the cathode material. Relative to the approximate center of the explosion at the cathode surface and within a few nanoseconds after its occurrence at $P = 100$ Torr, the emerged highly ionized cathode plasma expands spherically in the space near the cathode tip with a characteristic velocity of about 10^6 cm/s, which then decreases to values in the range of $\sim 10^5$–10^6 cm/s. The analysis of the cathode plasma expansion showed that, after the emergence on the lateral surface, the plasma gradually climbs up to the top of the point cathode, expands around the cathode tip resulting in a spherical region, and then remains concentrated around the cathode tip for several tens of nanoseconds (later stages were not studied in this research). No growth of any filaments with an electron density of $>10^{18}\text{cm}^{-3}$ from the cathode toward the anode is observed.

As a separate point, note that, when the pressure is reduced merely by several tens of Torr relative to the point of $P = 100$ Torr under the experimental conditions described above, the generation of highly ionized cathode plasma (with $N_e > 10^{18}\text{cm}^{-3}$) is not observed in principle, with the sensitivity of the used laser diagnosing techniques taken into account. Moreover, when the pressure is reduced relative to 100 Torr, the cathode plasma generation becomes sporadic from shot to shot, i.e., its generation could be or not, up to a certain pressure value at which its generation completely vanishes. Thus, we state that the generation of highly ionized cathode plasma, as in the case of the formation of microchannels, appears as a threshold phenomenon.

V. DISCUSSION OF THE EXPERIMENTAL RESULTS

A. Ionization processes and the generation of highly ionized plasma

According to the results of the theoretical and model analysis in Ref. [45], the evolution of the parameters of the considered pulsed nanosecond discharge in air occurs as follows. At the first stage (prebreakdown one), rapid shorting of the discharge gap by a streamer emerged near the point electrode (cathode) occurs [46,47]. As a result, a plasma channel with a relatively low degree of ionization and a radius of about 150–300 μm is formed between the electrodes. The appearance of such a weakly ionized plasma channel can also occur in a streamer-free discharge regime because of the intensive multiplication of electron avalanches during the rapid increase of the applied high-voltage pulse. These processes are clearly demonstrated in Refs. [10,48] by means of subnanosecond photography of a pulsed discharge, the parameters of which are close to those considered in the current study. The subsequent evolution of the parameters of the formed weakly ionized plasma channel can be described in the current approximation. In a relatively high electric field E/N (Td) and in the most part of the discharge gap there is an increase in the electron density and discharge current with a practically constant radius of the plasma channel. Then, near the cathode tip, where the current density and specific power of the energy input into the gas discharge medium are greater than in the mid-gap (due to the smaller radius of the channel), the discharge channel filamentation occurs alongside with the formation of a current channel (or channels) with a high degree of ionization–filaments.

At a high electron density, the time of the energy exchange between the electron and ion components of the plasma is sharply reduced [1]

$$\tau_{ei} = \frac{250 \times A_{\text{ion}} \times (T_e, \text{K})^{3/2}}{N_e \ln\Lambda}, \tag{7}$$

where $\ln\Lambda$ is the Coulomb logarithm, $A_{\text{ion}} = 14$ (for an ion N^+). At the electron concentration $N_e > 10^{19}\text{cm}^{-3}$ and temperature $T_e < 5\,\text{eV}$, the relaxation time does not exceed $\tau_{ei} < 1\,\text{ns}$, which agrees with the numerical results in Refs. [11,49]. Owing to the smallness of the value of τ_{ei}, a rapid equalization of the electron, ion, and translational temperatures of atoms and molecules occurs, so that the state of the plasma becomes close to local thermodynamic equilibrium. Note that, when estimating the electron-ion relaxation time in Eq. (7), we took the Coulomb logarithm value of $\ln\Lambda = 2$ for the observed plasma conditions (with $T_e = 3$–$4\,\text{eV}$ and n_e up to $5 \times 10^{19}\text{cm}^{-3}$), which satisfy the weakly nonideal plasma criterion. This estimation of the Coulomb logarithm for a weakly nonideal plasma was derived from numerical studies reported in Ref. [50], where $\ln\Lambda$ was evaluated from the calculated collision time curve for 532 nm wavelength at electron densities $n_e < 5 \times 10^{19}\text{cm}^{-3}$.

B. Explosive processes at the cathode and the generation of an ionization wave

Let us discuss the stage of the near-cathode plasma formation. In air at a pressure of 760 Torr its generation is accompanied by the appearance of a cathode spot with a transverse size of about 20 μm at a discharge current of about 100 A [30], which gives an estimate of the current density $j \sim 10^8\,\text{A/cm}^2$ in the spot region. At the stage of a developed channel, its diameter is about 200 μm with a current of approximately 300 A and a current density of $0.75 \times 10^6\,\text{A/cm}^2$. The normal current density in the cathode layer region at $P \leqslant 760$ Torr is $j_n \leqslant 120\,\text{A/cm}^2$ ($j_n \times P = 240\,\mu\text{A} \times \text{cm}^{-2} \times \text{Torr}^{-2}$) [1]. Hence, in the considered conditions, the discharge develops in a highly abnormal mode. As a result, one should expect a significant excess of the field in the cathode layer over the normal value and, accordingly, a significant increase in the probability of the explosive thermionic emission [1]. In addition, because of the electric field enhancement at microtips, a transition to the explosive electron emission is possible in the near-cathode region [43]. The characteristic lifetime of a fine-scale zone, wherein such a transition occurs, can be several tens of picoseconds [52]. The initiation of the transition to the explosive electron emission can be influenced by various dielectric films on the cathode surface, layers of adsorbed molecules and atoms of an air environment [53], as well as by the spatial charge of positive air ions concentrated around the tip of the point cathode [52]. As a result of a significant energy input into a relatively small area at the cathode, a certain part of the electrode material passes into the state of atomized metal plasma, which significantly reduces the potential barrier for the electron exit from the metal. During a time period comparable to a typical time of electron-phonon oscillations in metal, which is significantly shorter than typical times of the kinetic reactions in air plasma, a narrow region with a very high emission capacity arises. Through this region, a large number of electrons are injected into the air; it is assumed that electrons begin to leave the metal with an average thermal velocity of $v_{T_e} = \sqrt{kT_e/m_e} \sim 10^7$–$10^8$ cm/s at $T_e = 1$–$5\,\text{eV}$ [54]. The injected electron flow sharply increases the ionization of the air medium in the cathode region, which results in the formation of an ionization wave propagating toward the anode. We identify the position of the ionization wave front with the top of a growing highly ionized channel–a filament observed in the images in Figs. 2–4.

Note that in air at atmospheric pressure the frequency of electron-neutral collisions becomes less than the frequency of electron-ion collisions at $N_e > 10^{18}\text{cm}^{-3}$ [1,2]. So, the plasma channel conductivity depends weakly on N_e and is determined mainly by the electron temperature T_e [1], which ensures the conductivity in the channel behind the ionization wave front at a sufficiently high level. For example, at $T_e \approx 3\,\text{eV}$ and $N_e > 10^{18}\text{cm}^{-3}$ the plasma conductivity can be $\sigma_{ei} = N_e e^2/m_e \nu_{ei} \sim 200\ \text{Ohm}^{-1} \times \text{cm}^{-1}$. Owing to this, the channel's plasma is polarized very quickly, and the region with a high electric field is transferred to the top of the growing filament. It should be noted that a certain part of electrons (in the high-field zone) near the top of the growing filament can reach the runaway regime, but this effect is unlikely to have a significant impact on the discharge dynamics, since the filament growing occurs in the weakly ionized plasma medium formed between the electrodes at the prebreakdown stage.

Thus, the injection of a large number of electrons into the air under the condition of an explosion at the cathode,

wherein high gas and plasma temperatures are reached during extremely short time periods (compared to the plasma formation processes occurring far from the electrode), and a sharp increase in the ionization of the air medium are the key factors determining the formation of an ionization wave propagating toward the anode.

C. Electron density dynamics depending on the air pressure

The main processes that determine the characteristics of the filamentation mechanism at times of about 1 ns (at atmospheric pressure) are the stepwise dissociation of nitrogen molecules [55]

$$e + \mathrm{N_2} \rightarrow e + \mathrm{N_2}\left(A^3\Sigma_u^+, B^3\Pi_g, C^3\Pi_u\right), \tag{8}$$

$$e + \mathrm{N_2}\left(A^3\Sigma_u^+, B^3\Pi_g, C^3\Pi_u\right) \rightarrow e + \mathrm{N}(^4S) + \mathrm{N}(^2D), \tag{9}$$

and the stepwise ionization of the formed atomic particles

$$e + \mathrm{N}(^4S) \rightarrow e + \mathrm{N}(^2D, ^2P), \tag{10}$$

$$e + \mathrm{N}(^2D, ^2P) \rightarrow e + \mathrm{N^+} + e. \tag{11}$$

These processes result in a rapid increase in the electron density and a rapid heating of the gas.

Let us consider the dependence of the discharge filamentation time on the gas pressure in terms of the mechanism described by Eqs. (8)–(11). At relatively high fields, $E/N >$ 150 Td, efficient excitation of $\mathrm{N_2^{ex}} = \mathrm{N_2}(A^3\Sigma_u^+, B^3\Pi_g, C^3\Pi_u)$ by electron impact occurs. In air, at relatively low ionization degrees, the main quenching of $\mathrm{N_2^{ex}}$ is realized on oxygen molecules. However, with increasing an ionization degree, the dominant quenching channel becomes the electron impact dissociation of $\mathrm{N_2^{ex}}$; the reaction described by Eq. (9). At $E/N > 150$ Td this channel becomes the main one at $N_e/N \gg 4 \times 10^{-4}$. Oxygen molecules dissociate rapidly, resulting in a mixture dominated by nitrogen molecules ($\mathrm{N_2}$) and oxygen atoms (O). However, the contribution of direct atomic oxygen ionization to the overall electron production is significantly smaller than that of stepwise ionization processes involving $\mathrm{N_2}(A^3\Sigma_u^+, B^3\Pi_g, C^3\Pi_u)$ metastable states and nitrogen atoms (N) [45]. The $\mathrm{N}(^2D)$ atoms are either quenched upon collision with $\mathrm{N_2}$ and O or participate in stepwise ionization reactions (11).

According to Refs. [45,49], a rapid increase in the electron density (which determines the characteristic filamentation time of the discharge channel) begins after the main positive ions become atomic nitrogen ions, which have a relatively low electron-ion recombination coefficient. The dominance of $\mathrm{N^+}$ ions becomes possible only after reaching a sufficiently high dissociation degree of nitrogen molecules, $[\mathrm{N}_a]/[\mathrm{N_2}] > 1$ (where $[\mathrm{N}_a]$ and $[\mathrm{N_2}]$ are the concentrations of nitrogen atoms and molecules, respectively). If we assume that all the formed $\mathrm{N_2^{ex}}$ molecules participate in the stepwise dissociation reactions, then the rate of the atomic nitrogen production can be written as

$$d[\mathrm{N}_a]/dt = 2 \times k_{\mathrm{ex}} \times N_e \times [\mathrm{N_2}], \tag{12}$$

where k_{ex} is the rate constant of excitation of nitrogen molecules $\mathrm{N_2^{ex}}$ by electron impact in reaction (8). Then the characteristic time, at which the condition $[\mathrm{N}_a]/[\mathrm{N_2}] = 1$ is satisfied, will be

$$\tau_{\mathrm{ex}} = (2 \times k_{\mathrm{ex}} \times N_e)^{-1}. \tag{13}$$

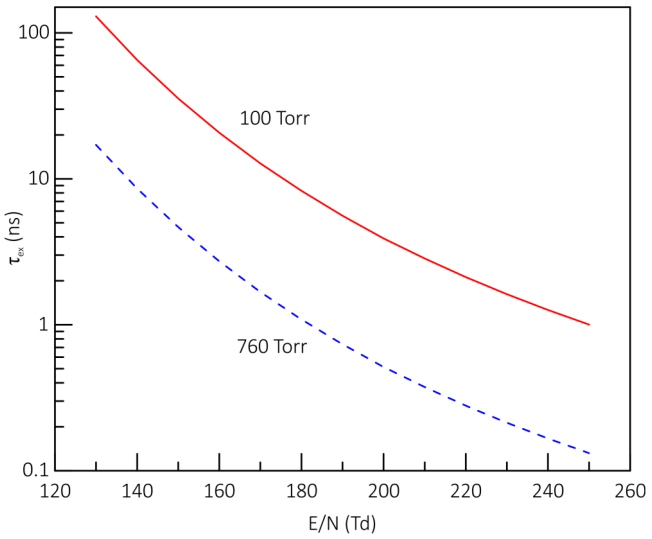

FIG. 9. Dependence of the filamentation time τ_{ex} on the reduced field E/N in air at $P = 100$ Torr and 760 Torr.

In this case, the electron density can be determined from the equation

$$N_e = \nu_{\mathrm{ion}}/k_{\mathrm{rec}}, \tag{14}$$

where ν_{ion} is the electron impact ionization frequency, and k_{rec} is the effective electron-ion recombination coefficient. From Eqs. (13) and (14) we obtain the relationship

$$\tau_{\mathrm{ex}} = (2 \times k_{\mathrm{ex}} \times \nu_{\mathrm{ion}}/k_{\mathrm{rec}})^{-1}. \tag{15}$$

Figure 9 shows the calculated dependence of the filamentation time τ_{ex} on the reduced field E/N described by Eq. (15). The calculations were performed with the assumption that at the initial stage of the discharge development the main positive ion will be $\mathrm{O_2^+}$ having the recombination coefficient $k_{\mathrm{rec}} = 2 \times 10^{-7} \times (300/T_e)^{0.7}\mathrm{cm^3/s}$ [56]. The ionization and excitation rates k_{ion} and k_{ex} were calculated as a function of a reduced electric field on the basis of the solution of the Boltzmann equation in a two-term approximation using BOLSIG+ code [57]. A self-consistent set of cross sections for electron collisions with $\mathrm{N_2}$ molecules were taken from Ref. [58], and for $\mathrm{O_2}$ molecules from Refs. [59,60], respectively.

Based on the data in Fig. 9, it can be assumed that it is the increase in the filamentation time with decreasing air pressure that is the main reason why at $P = 100$–200 Torr an extended filament with a high ionization degree does not have time to form, similar to that which forms at high pressures. Moreover, this effect occurs even when highly ionized plasma with high N_e, T_e, and T_i has already formed at the cathode. In other words, although explosive processes at the cathode do influence the emergence of an ionization wave in the direction to the anode, its development far from the electrode is not determined by the processes occurring in the near-cathode region, but is associated with the filamentation mechanism driven by the processes (8)–(11).

D. Specific energy input into the gas discharge medium

A distinctive feature of the created plasma, in addition to very high concentrations and temperatures of electrons, is the achievement of high gas pressures. This is a consequence of relatively short gas heating times τ_h, which do not exceed several nanoseconds [2,11], so that τ_h turn out to be significantly less than gas-dynamic times τ_g (gas pressure equalization times), $\tau_h \ll \tau_g$. Because of high gas temperatures and very small transverse dimensions (with radii $R \leqslant 30\,\mu$m) of a number of plasma channels, in the considered conditions characteristic gas-dynamic times can be $\tau_g = 10$–20 ns, which is confirmed by the data on the dynamics of the gas pressure in a spark channel presented in Ref. [51], wherein the pressure was decreased from 300 bar to 50 bar in approximately 20–25 ns. Note that, according to Ref. [51], the pressure in the channel becomes close to the atmospheric one only at times $>1\,\mu$s.

As we mentioned, at electron densities above $N_e > 10^{19}\text{cm}^{-3}$, the rapid equilibration of electron, ion, and neutral temperatures justifies treating the plasma as being in local thermodynamic equilibrium (LTE) with a unified temperature T. The experimental data obtained for nanosecond-contracted discharges in atmospheric air in Refs. [10,51,66] indicate a peak temperature of $T = 50 \pm 10$ kK. We can therefore estimate the corresponding specific energy input ϵ into the gas-discharge medium. Modeling the heating as a fast isochoric process, where the temperature rise is given by $\Delta T = (\gamma - 1)\epsilon/k$ (with k being Boltzmann's constant and γ the adiabatic index), and using $\gamma = 1.25$–1.3 for the high-pressure conditions ($P > 30$ bar) [67], we obtain an estimate for a specific energy input of $\epsilon = 14$–16 eV/molecule for $\Delta T = 50$ kK.

E. Fine-scale spark filamentation and the emergence of microchannels

Experimental measurements show that the head of a highly ionized filament is unstable and begins to break up into individual microchannels during the filament growing at a certain distance from the cathode tip. In air at 760 Torr, microchannels have typical diameters of the order of 20 μm, and the microchannel plasma can be close to a state of complete ionization at electron densities of $N_e = (1$–$5) \times 10^{19}\text{cm}^{-3}$ [16]. According to the research [19], in high-voltage discharges with a sharply nonuniform distribution of the electric field, the development of instabilities in the plasma and the formation of plasma microstructures in both the avalanche and plasma phases of the discharge are possible. In this regard, it is of interest to compare the observed transverse dimensions of the microchannels with the sizes of the heads of electron avalanches. In Ref. [1], it is shown that the growth of the transverse size of an avalanche head slows down and stops when its size becomes equal to α^{-1}, where $\alpha = \nu_{\text{ion}}/v_{\text{dr}}$ is the first Townsend coefficient and v_{dr} is the electron drift velocity in an air medium. According to the available experimental data on the dependence of $\nu_{\text{ion}}/v_{\text{dr}}$ on the value of E/N [61], at $E/N \leqslant 200$ Td we have $\nu_{\text{ion}}/v_{\text{dr}} \leqslant 4 \times 10^{-18}\text{cm}^2$. That is, at the air pressure $P = 760$ Torr and gas temperature $T_g = 300$ K we obtain $\alpha^{-1} \geqslant 100\,\mu$m, which is much larger than the experimentally measured radius of the observed microchannels. This fact indicates that the microchannel formation more likely occurs in the plasma phase of the discharge.

At present, however, there are no fundamental models or theoretical approaches that would explain the mechanism of the fine-scale spark filamentation—the splitting of a primary ionization wave into narrower plasma channels. The key difficulties here are stipulated by a large number of factors that need to be taken into account when describing the fine-scale spark filamentation process. Let us clarify that a detailed examination of the well-known instabilities such as ion-acoustic, Buneman, and filamentation (a special case of a two-stream instability) instabilities, which successively transform into each other [62–65], has not yet given a comprehensive answer to the question of what initiates the filamentation process and how it is carried out. A certain challenge consists in the need to consider the ionization wave propagation in a weakly ionized plasma channel formed between the electrodes at the prebreakdown stage of the discharge. After the gap breakdown, the discharge voltage drops sharply to units of kV, i.e., microchannels propagate under conditions of a relatively low field E/N.

Thus, the description of the fine-scale spark filamentation mechanism is an open problem requiring further investigation. In addition, one should take into account the threshold nature of this phenomenon, which consists in the fact that the formation of a microchannel system ceases to be observed when the air pressure decreases from 400 to 300 Torr.

VI. CONCLUSION

In conclusion, let us briefly outline the key findings. To maintain the generality of the results obtained, we formulate some states based on the data obtained earlier in previous studies.

(1) The generation of highly ionized plasma in the discharge bulk (in the case of millimeter-sized gaps) at all considered pressures (100–760 Torr) is observed starting from the gap breakdown only.

(2) Explosive processes at the cathode influence the emergence of an ionization wave propagating toward the anode. The propagation velocity of the wave is practically independent of the air pressure.

(3) At high pressures, $P = 400$–760 Torr, the ionization wave front is unstable and breaks up into many microchannels—the fine-scale spark filamentation process runs. Microchannels have typical diameters of $\sim 20\,\mu$m and high electron densities, $N_e = (1$–$5) \times 10^{19}\text{cm}^{-3}$.

(4) The formation of microchannels ceases to be observed when the air pressure decreases from 400 to 300 Torr. The development of the discharge occurs mainly through the formation of a homogeneous highly ionized filament.

(5) When the pressure decreases from 760 to 200 Torr, a gradual decrease in the maximum electron density is observed, although maximum electron density values $N_e^{\max}$ themselves are quite high, $N_e > 10^{19}\text{cm}^{-3}$, and correspond to almost complete ionization of the resultant atomic particles.

(6) The generation of highly ionized near-cathode plasma at $P = 100$ Torr has an explosive nature and is not observed when the air pressure decreases (by several tens of Torr) below 100 Torr.

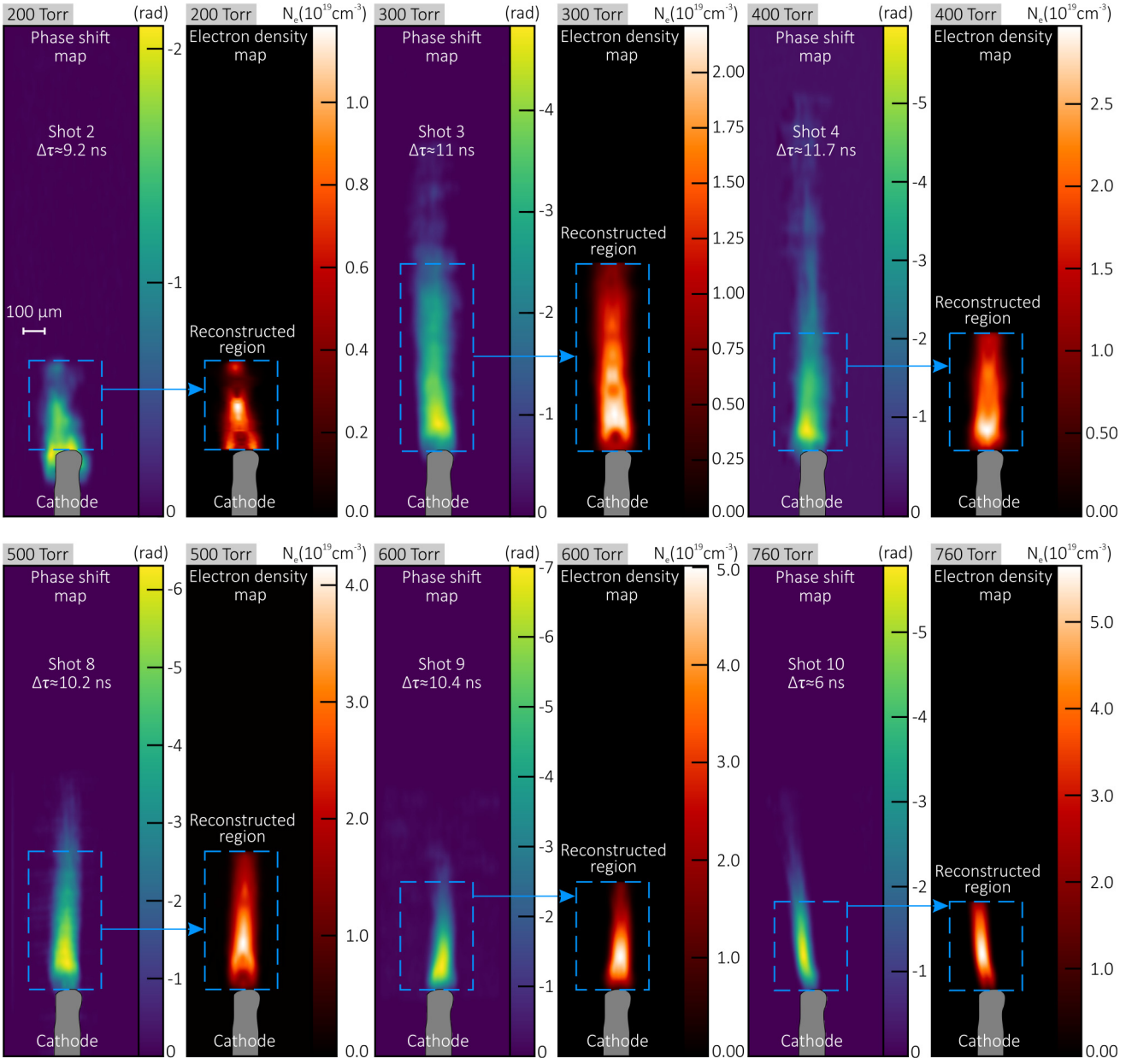

FIG. 10. Phase shift and reconstructed electron density maps obtained for shots 1–3 and 8–10. The maps illustrate filaments developing at different pressures 100–760 Torr from the point cathode and their sections selected for processing.

(7) The filamentation time increases with decreasing air pressure, which can be the reason for the observed structural changes in the development of the discharge channel.

Threshold effects associated with the generation of highly ionized plasma channels in a pulsed nanosecond discharge in air are important for creating consistent concepts of plasma formation processes and refining already developed models of plasma-chemical kinetics. The experimental and theoretical data on ionization processes in pulsed spark discharges obtained in the research are also valuable for a broad range of studies on various types of ionization waves [68–70]. The advancement of scientific knowledge in this area is also relevant for studies of long spark discharges initiated by megavolt voltage pulses, which is important within the framework of laboratory modeling the processes that occur in real lightning. So, obtaining new experimental data in this research field is a pressing task. In the current research, with a high temporal and spatial resolution, we studied in detail the features of the development of a pulsed nanosecond discharge depending on the air pressure in the range from units of Torr to 760 Torr. The findings obtained provide new insights into the physics behind the ionization processes and fundamental structural changes taking place in the development of a resultant discharge channel. Note specially that the generation of highly ionized near-cathode plasma at pressures of the order of 100–200 Torr can be of interest for such applied fields of a pulsed nanosecond gas discharge as the production of metal nanoparticles formed at the end of the discharge.

TABLE I. Estimated plasma parameters for the filament sections identified in Fig. 10. The parameters are defined as follows: Δt is the moment of consideration. $E_{\text{sum}} = \epsilon n_i/2$ is the total energy required to generate a highly ionized plasma. n_i is the ion number density. $\epsilon \approx 16$ eV/molecule is the effective specific energy input. $\delta(n_i)$ is the estimated uncertainty of n_i. V is the volume of the analyzed filament segment. $n_m = N_a P_0 V/RT_0$ is the molecula number existing in the volume V in ordinaty air at $P_0 = 760$ Torr and $T_0 = 300$ K. N_a is the Avogadro constant, and R is the molar gas constant. I is the total current throught the discharge gap. j is the mean current density averaged over the considered filament section. r is the mean radius of the channel across the selected filament section. Q is the total electrical energy deposited into the discharge gap. N_e^{thr} is the electron density obtained from complete dissociation and single ionization of air particles.

	Shot 2	Shot 3	Shot 4	Shot 8	Shot 9	Shot 10
P [Torr]	200	300	400	500	600	760
n_i [counts]	3.44×10^{13}	2.11×10^{14}	1.5×10^{14}	1.59×10^{14}	1.02×10^{14}	6.45×10^{13}
$\Delta(n_i)$ [%]	≈7.3	≈3.7	≈6	≈4.3	≈3.5	≈2.2
V [μm^3]	9.5×10^6	2.8×10^7	1.8×10^7	1.1×10^7	6×10^6	3×10^6
n_i/n_m [arb. units]	≈0.562	≈0.78	≈0.647	≈0.898	≈0.88	≈0.879
E_{sum} [μJ]	≈44	≈270	≈192	≈204	≈130	≈83
Q [mJ]	≈4.2	≈5.2	≈7.3	≈6.7	≈9.3	≈4.8
Δt [ns]	9.2 ± 0.1	11 ± 0.1	11.7 ± 0.1	10.2 ± 0.1	10.4 ± 0.1	6 ± 0.1
I [A]	≈268	≈257	≈262	≈250	≈249	≈240
j [A/cm^2]	$\approx 1.127 \times 10^6$	$\approx 0.9 \times 10^6$	$\approx 1 \times 10^6$	$\approx 1.13 \times 10^6$	$\approx 2 \times 10^6$	$\approx 3.18 \times 10^6$
r [μm]	87 ± 15	95 ± 26	91 ± 5	78 ± 4	63 ± 7	49 ± 2
N_e^{thr} [cm^{-3}]	1.42×10^{19}	2.13×10^{19}	2.84×10^{19}	3.55×10^{19}	4.26×10^{19}	5.4×10^{19}

ACKNOWLEDGMENT

The study was supported by the Russian Science Foundation (Grant No. 24-79-10167).

DATA AVAILABILITY

The data are not publicly available. The data are available from the authors upon reasonable request.

APPENDIX: SUPPLEMENTARY DATA

Figure 10 presents phase shift maps obtained by processing interferograms of the filaments (spark channels) in shots 1–3 and 8–10 registered in the pressure range of 100–760 Torr. For each phase map, we identified the filament region most amenable to accurate processing and reconstruction of the electron density (i.e., solving the inverse diffraction problem). For these corresponding regions, the reconstructed electron density distributions are displayed as 2D maps of 3D axisymmetric plasma objects (recall that the problem was solved under the axial symmetry approximation). The filament sections were selected based on the following criteria:

(1) The maximum electron density should not exceed the threshold (N_e^{thr}) for complete single ionization and dissociation. This reliably excludes the contribution of cathode metal vapors, which could augment the plasma's electron component.

(2) The selected channel section must exhibit axial symmetry or be symmetrizable with a minimal error (i.e., no microstructure or strong inhomogeneity in the channel cross-section). This is essential for correctly solving the inverse problem.

For the selected channel sections, the total number of ions, n_i, was calculated with an uncertainty of ≈7% or less. This value does not exceed the original number of air molecules, n_m, that occupied the same volume V under normal conditions. The corresponding data are listed in Table I for the channels' sections registered in the shots presented in Fig. 10. Consequently, we conclude that the ion population in the selected region is dominated by ions originating from air particles. This argument, however, is challenged by the near-cathode plasma formed at $P = 100$ Torr, which consists primarily of the ionized cathode vapor [42].

The formation of the highly ionized plasma in the specified regions constitutes a very small fraction of the total energy input. Based on the estimate of the specific energy input into the gas-discharge medium (in Sec. V D), one can take its value to be $\epsilon = 16$ eV/molecule and use this value to estimate a characteristic total energy $E_{\text{sum}} = \epsilon n_i/2 \sim 40 - 270$ μJ required to create the plasma in the selected volumes V. The total electrical energy $Q \approx \int_{t_{\text{br}}}^{\Delta t} U(t)I(t)dt$ deposited into the discharge gap by the time Δt of the plasma observation is typically about 4–10 mJ; see Fig. 11. The initial energy stored in the cable generator is $CU^2/2 \approx 335$ mJ, wherein the total capacitance C is derived from a specific capacitance of 67 pF/m for the 75 Ω cable with a length of 4 m.

For reference, in Table I we also provide additional plasma and discharge parameters relevant for further analysis. These include the filament volume V of the processed region, the current I and the average current density j in the channel at

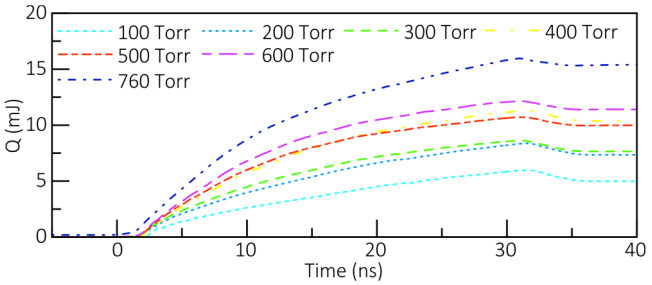

FIG. 11. Total electrical energy Q deposited into the discharge gap for shots given in Table I.

the observation time Δt (under the assumption that all current flows through the highly ionized channel), and the average channel radius r (calculated over the entire selected filament area).

[1] Y. P. Raizer and J. E. Allen, *Gas Discharge Physics* (Springer, Berlin, 1997), Vol. 2.

[2] T. Orrie're, E. Moreau, and D. Z. Pai, Ionization and recombination in nanosecond repetitively pulsed microplasmas in air at atmospheric pressure, J. Phys. D **51**, 494002 (2018).

[3] N. Q. Minesi, P. B. Mariotto, E. Pannier, A. Vincent Randonnier, G. D. Stancu, and C. O. Laux, Kinetic mechanism and sub-ns measurements of the thermal spark in air, Plasma Sources Sci. Technol. **32**, 044005 (2023).

[4] D. Levko and L. L. Raja, Kinetics of the fast ionization waves with runaway electrons, Phys. Plasmas **30**, 073502 (2023).

[5] M. Medvedev, E. Parkevich, A. Oginov, S. Zakharov, and I. Baidin, Internal microstructure of current channel of the long spark discharge, Bull. Lebedev Phys. Inst. **48**, 373 (2021).

[6] S. Huang, W. Chen, Z. Fu, Y. Fu, N. Xiang, X. Qiu, W. Shi, D. Cheng, and Z. Zhang, Separate luminous structures leading positive leader steps, Nat. Commun. **13**, 3655 (2022).

[7] X. Zhao, N. A. Popov, Q. Gan, Y. Ding, Y. Du, and J. He, On a possible mechanism of space stem formation in negative long sparks, Geophys. Res. Lett. **50**, e2023GL102834 (2023).

[8] Y. Li, S. S. Li, Y. Feng, S. M. Qie, H. Yuan, and D. Z. Yang, Fast breakdown process and characteristics diagnosis of nanosecond pin–pin discharge, J. Phys. D **57**, 225201 (2024).

[9] Y. Liu, T. Silva, T. C. Dias, P. Viegas, X. Zhao, Y. Du, J. He, and V. Guerra, An updated set of electronimpact cross sections for CO_2: Untangling dissociation and application to CO_2 with Ar and N_2 admixtures, Plasma Sources Sci. Technol. **34**, 035003 (2025).

[10] N. Minesi, S. Stepanyan, P. Mariotto, G. D. Stancu, and C. O. Laux, Fully ionized nanosecond discharges in air: The thermal spark, Plasma Sources Sci. Technol. **29**, 085003 (2020).

[11] S. Shcherbanev, C. Ding, S. Starikovskaia, and N. Popov, Filamentary nanosecond surface dielectric barrier discharge: Plasma properties in the filaments, Plasma Sources Sci. Technol. **28**, 065013 (2019).

[12] C. Ding, A. Jean, N. Popov, and S. Starikovskaia, Fine structure of streamer-to-filament transition in highpressure nanosecond surface dielectric barrier discharge, Plasma Sources Sci. Technol. **31**, 045013 (2022).

[13] A. Brisset, T. Guenin, P. Tardiveau, and A. Sobota, Electron density and temperature in a diffuse nanosecond pulse discharge in air at atmospheric pressure, Plasma Sources Sci. Technol. **32**, 065014 (2023).

[14] K. Almazova, A. Belonogov, V. Borovkov, V. Kurbanismailov, Z. Khalikova, P. K. Omarova, G. Ragimkhanov, D. Tereshonok, and A. Trenkin, Investigation of the microchannel structure in the initial phase of the discharge in air at atmospheric pressure in the 'pin (anode)-plane' gap, Phys. Plasmas **27**, 123507 (2020).

[15] K. I. Almazova, A. N. Belonogov, V. V. Borovkov, V. S. Kurbanismailov, G. B. Ragimkhanov, A. A. Tren'kin, D. V. Tereshonok, and Z. R. Khalikova, Plasma and gas-dynamic near-electrode processes in the initial phase of a microstructured spark discharge in air, Tech. Phys. Lett. **46**, 737 (2020).

[16] E. Parkevich, M. Medvedev, G. Ivanenkov, A. Khirianova, A. Selyukov, A. Agafonov, P. A. Korneev, S. Gus'Kov, and A. Mingaleev, Fast fine-scale spark filamentation and its effect on the spark resistance, Plasma Sources Sci. Technol. **28**, 095003 (2019).

[17] A. Perminov and A. Tren'kin, microstructure of the current channels in a nanosecond spark discharge in atmospheric-pressure air in uniform and highly nonuniform electric fields, Tech. Phys. **50**, 1158 (2005).

[18] V. Karelin and A. Tren'kin, self-similar spatial structure of a streamer-free nanosecond discharge, Tech. Phys. **53**, 314 (2008).

[19] V. Karelin and A. Tren'kin, formation of the microscopic structure of high-voltage nanosecond diffuse discharges in sharply nonuniform geometry, Tech. Phys. **53**, 1236 (2008).

[20] E. Parkevich and A. Khirianova, On the possible threshold character of the spark microstructure formation, Bull. Lebedev Phys. Inst. **49**, 302 (2022).

[21] A. Tren'kin, K. Almazova, A. Belonogov, V. Borovkov, E. Gorelov, I. Morozov, and S. Y. Kharitonov, Influence of preionization on the microchannel structure of a spark discharge in air in a pin-plane gap, Tech. Phys. **68**, S493 (2023).

[22] A. A. Tren'kin, K. I. Almazova, A. N. Belonogov, V. V. Borovkov, A. S. Dolotov, and I. V. Morozov, Dynamics of structure of pulsed discharge in nitrogen and argon at different pressures in a 'pin to plane' gap, Tech. Phys. **69**, 431 (2024).

[23] E. Parkevich, M. Medvedev, A. Selyukov, A. Khirianova, A. Mingaleev, S. Mishin, S. Pikuz, and A. Oginov, Setup involving multi-frame laser probing for studying fast plasma formation with high temporal and spatial resolutions, Opt. Lasers Eng. **116**, 82 (2019).

[24] E. Parkevich, M. Medvedev, A. Selyukov, A. Khirianova, A. Mingaleev, and A. Oginov, Laser-triggered gas switch with sub-nanosecond jitter and breakdown delay tunable over 0.1–10 ns governed by the spark gap ignition angle, Plasma Sources Sci. Technol. **29**, 05LT03 (2020).

[25] E. Parkevich, A. Khiryanova, T. Khiryanov, D. Tolbukhin, Y. K. Bolotov, and S. Ambrozevich, On the quantitative evaluation of laser diffraction by plasma formations with a micron-sized diameter, Bull. Lebedev Phys. Inst. **50**, 540 (2023).

[26] G. Sarkisov, Shearing interferometer with an air wedge for the electron density diagnostics in a dense plasma, Instrum. Exp. Tech. **39**, 727 (1996).

[27] S. Pikuz, V. Romanova, N. Baryshnikov, M. Hu, B. Kusse, D. Sinars, T. Shelkovenko, and D. Hammer, A simple air wedge shearing interferometer for studying exploding wires, Rev. Sci. Instrum. **72**, 1098 (2001).

[28] A. I. Khirianova, E. V. Parkevich, M. A. Medvedev, T. F. Khirianov, and A. S. Selyukov, Algorithm of interferogram tracing. II. Fringes with negative curvature and extended approach to their processing, J. Russ. Laser Res. **42**, 161 (2021).

[29] T. F. Khirianov, A. I. Khirianova, E. V. Parkevich, and I. Makarov, *WISP: Workframe for Interferogram Signal Phase-Unwrapping* (IEEE Access, New York, 2025).

[30] E. Parkevich, G. Ivanenkov, M. Medvedev, A. Khirianova, A. Selyukov, A. Agafonov, A. Mingaleev, T. Shelkovenko, and S. Pikuz, Mechanisms responsible for the initiation of a fast breakdown in an atmospheric discharge, Plasma Sources Sci. Technol. **27**, 11LT01 (2018).

[31] R. N. Bracewell, Strip integration in radio astronomy, Aust. J. Phys. **9**, 198 (1956).

[32] E. Parkevich, M. Medvedev, A. Khirianova, G. Ivanenkov, A. Selyukov, A. Agafonov, K. Shpakov, and A. Oginov, Extremely fast formation of anode spots in an atmospheric discharge points to a fundamental ultrafast breakdown mechanism, Plasma Sources Sci. Technol. **28**, 125007 (2019).

[33] E. Parkevich, Features of the structure of spark channels in a near-cathode region, JETP Lett. **120**, 489 (2024).

[34] E. V. Parkevich, A. Khirianova, T. Khirianov, K. V. Shpakov, K. T. Smaznova, Y. K. Bolotov, and S. Ambrozevich, Parameters of electric spark microchannels in the near-anode region of the discharge, Bull. Lebedev Phys. Inst. **50**, S1283 (2023).

[35] C. Vest, Interferometry of strongly refracting axisymmetric phase objects, Appl. Opt. **14**, 1601 (1975).

[36] U. Kogelschatz and W. Schneider, Quantitative schlieren techniques applied to high current arc investigations, Appl. Opt. **11**, 1822 (1972).

[37] K. I. Almazova, A. N. Belonogov, V. V. Borovkov, *et al.*, Investigation of the dynamics of a microstructured spark channel in air in the "tip (anode)–plane" geometry at the stage of radial expansion, Plasma phys. Rep, **47**, 73 (2021).

[38] K. I. Almazova, A. A. Amirova, A. N. Belonogov, *et al.*, Microchannel structure parameters in the initial phase of a spark discharge in a tip–plane gap in atmospheric-pressure air, Tech. Phys. Lett. **47**, 71 (2021).

[39] E. V. Parkevich, A. I. Khirianova, T. F. Khirianov, K. T. Smaznova, D. V. Tolbukhin, V. M. Romanova, I. A. Kozin, and S. A. Ambrozevich, Strong diffraction effects accompany the transmission of a laser beam through inhomogeneous plasma microstructures, Phys. Rev. E **109**, 055204 (2024).

[40] G. Mesyats, E. Parkevich, S. Pikuz, and M. Yalandin, Shunting effect in explosive electron emission, in *Doklady Physics* (Springer, Berlin, 2016), Vol. 61, p. 481.

[41] S. A. Pikuz, T. A. Shelkovenko, I. N. Tilikin, E. V. Parkevich, A. R. Mingaleev, A. V. Agafonov, and D. A. Hammer, Studying of explosive electron emission from 'whisker' cathode using x-ray point-projection radiography, IEEE Trans. Plasma Sci. **46**, 3815 (2018).

[42] K. S. E. V. Parkevich and A. I. Khirianova, On the parameters of the cathode plasma arising during the breakdown of millimeter air gaps at low pressures, Bull. Lebedev Phys. Inst. **52**, 213 (2025).

[43] Y. D. Korolev and G. A. Mesyats, *Field Emission and Explosive Processes in a Gas Discharge [in Russian]* (Nauka, Novosibirsk, 1982).

[44] S. Barengolts, G. Mesyats, and M. Tsventoukh, Initiation of ecton processes by interaction of a plasma with a microprotrusion on a metal surface, J. Exp. Theor. Phys. **107**, 1039 (2008).

[45] B. Zhang, Y. Zhu, X. Zhang, N. Popov, T. Orri'ere, D. Z. Pai, and S. M. Starikovskaia, Streamer-to-filament transition in pulsed nanosecond atmospheric pressure discharge: 2D numerical modeling, Plasma Sources Sci. Technol. **32**, 115014 (2023).

[46] V. F. Tarasenko, D. V. Beloplotov, M. I. Lomaev, D. A. Sorokin, *et al.*, Features of streamer formation in a sharply non-uniform electric field, J. Appl. Phys. **125**, 244501 (2019).

[47] D. Beloplotov, V. Tarasenko, D. Sorokin, C. Zhang, and T. Shao, Positive and negative streamers in air and nitrogen in a sharply inhomogeneous electric field under conditions of runaway electron generation, High Voltage **8**, 527 (2023).

[48] N. Minesi, S. A. Stepanyan, P. B. Mariotto, G. D. Stancu, and C. O. Laux, On the arc transition mechanism in nanosecond air discharges, in *Proceedings of the AIAA Scitech Forum* (American Institute of Aeronautics and Astronautics, Inc., San Diego, California, 2019), p. 463.

[49] N. Minesi, P. Mariotto, E. Pannier, G. D. Stancu, and C. O. Laux, The role of excited electronic states in ambient air ionization by a nanosecond discharge, Plasma Sources Sci. Technol. **30**, 035008 (2021).

[50] A. Bataller, B. Kappus, C. Camara, and S. Putterman, Collision time measurements in a sonoluminescing microplasma with a large plasma parameter, Phys. Rev. Lett. **113**, 024301 (2014).

[51] H. Albrecht, W. Bloss, W. Herden, R. Maly, B. Saggau, and E. Wagner, New aspects on spark ignition, SAE Tech. Paper 770853 (1977).

[52] N. M. Zubarev and G. A. Mesyats, Initiation of explosive electron emission and runaway of electrons during pulsed breakdown of dense gases, JETP Lett. **113**, 259 (2021).

[53] Y. A. Barengolts, Potential barrier decrease at cathode boundary under high-voltage gas-discharge conditions, Tech. Phys. Lett. **38**, 218 (2012).

[54] G. A. Mesyats and D. I. Proskurovsky, *Pulsed Electrical Discharge in Vacuum* (Springer-Verlag, Berlin, 1989).

[55] T. L. Chng, N. D. Lepikhin, I. S. Orel, N. A. Popov, and S. M. Starikovskaia, TALIF measurements of atomic nitrogen in the afterglow of a nanosecond capillary discharge, Plasma Sources Sci. Technol. **29**, 035017 (2020).

[56] A. Florescu-Mitchell and J. B. A. Mitchell, Dissociative recombination, Phys. Rep. **430**, 277 (2006).

[57] G. Hagelaar and L. C. Pitchford, Solving the Boltzmann equation to obtain electron transport coefficients and rate coefficients for fluid models, Plasma Sources Sci. Technol. **14**, 722 (2005).

[58] A. V. Phelps and L. C. Pitchford, Anisotropic scattering of electrons by N_2 and its effect on electron transport, Phys. Rev. A **31**, 2932 (1985).

[59] O. Braginskiy, A. Vasilieva, K. Klopovskiy, A. Kovalev, D. Lopaev, O. Proshina, T. Rakhimova, and A. Rakhimov, Singlet oxygen generation in O_2 flow excited by RF discharge: I. Homogeneous discharge mode: α-mode, J. Phys. D **38**, 3609 (2005).

[60] A. Kovalev, D. Lopaev, Y. A. Mankelevich, N. Popov, T. Rakhimova, A. Y. Poroykov, and D. Carroll, Kinetics of $O_2\, b^1 \sum_g^+$) In oxygen RF discharges J. Phys. D: Appl. Phys. **38**, 2360 (2005).

[61] G. G. Raju, *Gaseous Electronics: Tables, Atoms, and Molecules* (CRC Press, Boca Raton, FL, 2018).

[62] A. Weingarten, S. Alexiou, Y. Maron, M. Sarfaty, Y. E. Krasik, and A. S. Kingsep, Observation of nonthermal turbulent electric

fields in a nanosecond plasma opening switch experiment, Phys. Rev. E **59**, 1096 (1999).

[63] K. Tsigutkin, R. Doron, E. Stambulchik, V. Bernshtam, Y. Maron, A. Fruchtman, and R. J. Commisso, Electric fields in plasmas under pulsed currents, Phys. Rev. E **76**, 046401 (2007).

[64] B. Hao, Z. M. Sheng, and J. Zhang, Kinetic theory on the current-filamentation instability in collisional plasmas, Phys. Plasmas **15**, 082112 (2008).

[65] A. Bret, WEIBEL, two-stream, filamentation, oblique, Bell, Buneman... Which one grows faster? Astrophys. J. **699**, 990 (2009).

[66] L. A. Cessou, *et al.*, Streamer-to-spark transition initiated by a nanosecond overvoltage pulsed discharge in air, Plasma Sources Sci. Technol. **26**, 045012 (2017).

[67] M. Capitelli, *et al.*, *Fundamental Aspects of Plasma Chemical Physics* (Springer, New York, NY, 2016).

[68] L. M. Vasilyak, *et al.*, Fast ionisation waves under electrical breakdown conditions, Phys. Usp. **37**, 247 (1994).

[69] V. A. Rakov and M. A. Uman, *Lightning: Physics and Effects* (Cambridge University Press, Cambridge, UK, 2003).

[70] Z. Xiong, *et al.*, Dynamics of ionization wave splitting and merging of atmospheric-pressure plasmas in branched dielectric tubes and channels, J. Phys. D **45**, 275201 (2012).